



HAL
open science

Active rejection-enhancement of spectrally tunable liquid crystal geometric phase vortex coronagraphs

Nina Kravets, Urban Mur, Miha Ravnik, Slobodan Žumer, Etienne Brasselet

► **To cite this version:**

Nina Kravets, Urban Mur, Miha Ravnik, Slobodan Žumer, Etienne Brasselet. Active rejection-enhancement of spectrally tunable liquid crystal geometric phase vortex coronagraphs. Applied Physics Letters, 2022, 121 (24), pp.241104. 10.1063/5.0130078 . hal-04104056

HAL Id: hal-04104056

<https://hal.science/hal-04104056>

Submitted on 23 May 2023

HAL is a multi-disciplinary open access archive for the deposit and dissemination of scientific research documents, whether they are published or not. The documents may come from teaching and research institutions in France or abroad, or from public or private research centers.

L'archive ouverte pluridisciplinaire **HAL**, est destinée au dépôt et à la diffusion de documents scientifiques de niveau recherche, publiés ou non, émanant des établissements d'enseignement et de recherche français ou étrangers, des laboratoires publics ou privés.

Active rejection-enhancement of spectrally tunable liquid crystal geometric phase vortex coronagraphs

Cite as: Appl. Phys. Lett. **121**, 241104 (2022); doi: [10.1063/5.0130078](https://doi.org/10.1063/5.0130078)

Submitted: 9 October 2022 · Accepted: 5 December 2022 ·

Published Online: 14 December 2022



View Online



Export Citation



CrossMark

Nina Kravets,¹ Urban Mur,² Miha Ravnik,^{2,3} Slobodan Žumer,^{2,3} and Etienne Brasselet^{1,a)}

AFFILIATIONS

¹Université de Bordeaux, CNRS, Laboratoire Ondes et Matière d'Aquitaine, F-33400 Talence, France

²Faculty of Mathematics and Physics, University of Ljubljana, Jadranska 19, 1000 Ljubljana, Slovenia

³Jožef Stefan Institute, Jamova 39, 1000 Ljubljana, Slovenia

^{a)} Author to whom correspondence should be addressed: etienne.brasselet@u-bordeaux.fr

ABSTRACT

Geometric phase optical elements made of space-variant anisotropic media customarily find their optimal operating conditions when a half-wave retardance condition is fulfilled, which allows imparting polarization-dependent changes to an incident wavefront. In practice, intrinsic limitations of a man-made manufacturing process or a finite spectrum of a light source lead to a deviation from the ideal behavior. This implies an implementation of strategies to compensate for the associated efficiency losses. Here, we report on how the intrinsic tunable features of self-engineered liquid crystal topological defects can be used to enhance rejection capabilities of spectrally tunable vector vortex coronagraphs. We also discuss the extent of which current models enable to design efficient devices. The simplicity and decent performance of our approach offer the possibility to an amateur astronomy community to consider the use of vortex coronagraphy.

Published under an exclusive license by AIP Publishing. <https://doi.org/10.1063/5.0130078>

Liquid crystal optical devices usually modulate a phase and/or a polarization state of light by electrically driven changes in an orientational state of the material along a light propagation direction. The transverse degrees of freedom bring additional options for phase modulation. This is the case for liquid crystal slabs whose orientational state (defined locally by the average molecular orientation defined by a unit vector \mathbf{n} called director) imparts a half-wave birefringent retardation to an incident light field along its propagation direction and space-variant phase profile of a geometric nature in the transverse plane. Their complex amplitude transfer function is given as $t = \exp(\pm 2i\psi)$, where the \pm sign refers to the handedness of the incident circular polarization state and ψ is the effective in-plane optical axis orientation angle. Such geometric phase optical elements were anticipated in the late 1990s¹ and experimentally realized a few years after using space-variant solid-state subwavelength gratings^{2,3} followed by the advent of their liquid crystal counterparts.^{4,5}

Here, we deal with liquid crystal geometric phase optical vortex masks ideally associated with $t = \exp(\pm 2im\phi)$, where m is an integer or half-integer and ϕ is the polar angle in the (x, y) plane of the optical element, which were introduced in 2006.⁵ To date, there is a trade-off between (i) the tunability of the operating wavelength satisfying the

half-wave plate condition, which is achieved either by thermal⁶ or electrical⁷ means and (ii) the spatial resolution of the structural singularity for the director orientation that can reach sub-micrometer size.⁸ Since most applications involve optical beams with cross sections in the millimeter range or larger, they do not suffer from such a compromise. However, this is *a priori* no longer true when the geometric phase vortex mask is required in the focal plane of an optical system, as is the case for vector optical vortex coronagraphy.

Optical coronagraphy is a high contrast imaging technique initially developed to create artificial total eclipses of the Sun.⁹ The working principle of the original apparatus is to occult the central part of the Airy diffraction pattern in the Fourier plane of a telescope in order to strongly reduce the amount of on-axis stellar light reaching the observer. It was not until nearly 60 years later that the (binary) manipulation of the phase of the Airy spot rather than its occultation was considered.¹⁰ Further developments led to the advent of optical vortex coronagraphy, where a vortex phase mask is centered on the Airy pattern of the on-axis light source to be rejected. Scalar and vector coronagraphy have been proposed simultaneously in Refs. 11 and 12. Their respective labels refer to the physical origin of the phase changes operated by the vortex phase mask: dynamic (scalar case) or geometric (vector case).

Nowadays, more than one decade after first laboratory¹³ and astronomical^{14,15} demonstrations, *spectrally static* geometric phase vortex masks equip several ground based astronomical observations facilities¹⁶ and recent progresses suggest their future use in space telescopes.¹⁷

Importantly, spectroscopic imaging of extrasolar planets to learn about their atmospheric composition involves developing broadband vortex masks. This inherently comes with polarization leakage problems and requires demanding technological improvements to mitigate the effects, not only for the vortex mask itself but also for the additional polarization optics involved.^{18,19} Another approach would be to consider *spectrally tunable* geometric phase vortex masks that do not require the use of additional polarization optics and to use them in a narrowband regime while the operating wavelength is scanning the desired spectral bandwidth. However, the spectrally tunable options reported so far remain hampered by central disorientation region trade-off.^{20–22} There are two distinct kinds of central disorientation in liquid crystal geometric phase vortex masks: (i) the departure from the space-variant pattern $\psi = m\phi$ (to an unimportant constant) and (ii) the departure from the half-wave birefringent retardance, which could mix in practice. The few previous attempts can be classified as being mainly either on type (i)²² or type (ii).^{20,21} In the first case, it is difficult to consider post-reprogramming of the fabrication-limited patterned anchoring layers that provide a liquid crystal alignment. Nevertheless, the placement of an opaque disk covering the troublesome region is a rough solution applicable regardless of the nature of the vortex mask.¹⁴ In the second case, which refers to the use of spontaneously formed liquid crystal topological defects under the action of external fields, an additional backup option consists to place the vortex mask between crossed circular polarizers at the expense of throughput losses of at least 50% for unpolarized light observations as well as chromatic issues of the additional polarization optics.

In order to get rid of obstruction and polarization filtering backup strategies for type (ii) vortex masks, it has been suggested that tuning the size of the disorientation region is an open option when using liquid crystal topological defects called umbilics,²⁴ which we quantitatively explored experimentally in the present work. Also, we discuss the capabilities of available analytical model and full numerical simulation as tools toward optimal design. Umbilics are nonsingular topological defects associated with $m = \pm 1$ unveiled 40 years ago by Rapini²⁵ in nematic liquid crystals having negative dielectric anisotropy ($\epsilon_a < 0$) and sandwiched between two parallel substrates providing uniform perpendicular orientational boundary conditions for the director $[\mathbf{n}(x, y, z = 0) = \mathbf{n}(x, y, z = L) = \mathbf{e}_z]$, where L is the cell thickness and \mathbf{e}_z is the unit vector along the z axis. These defects spontaneously appear when applying a quasistatic voltage between the two facets of the nematic slab that exceeds the Fréedericksz threshold value $U_{th} = \pi\sqrt{K_3}/(\epsilon_0|\epsilon_a|)$, where K_3 is the bend elastic constant of the nematic and ϵ_0 is the vacuum dielectric permittivity.²⁵ In our experiments, we used a 20 μm -thick sample prepared with the dual frequency nematic mixture 1859A (from Military University of Technology, Warsaw, Poland) and umbilics are obtained following the magnetic–electric approach proposed in Ref. 24 [see Figs. 1(a) and 1(b)]. The combined action of a static magnetic field from a ring magnet with a quasistatic electric field (square waveform at 200 kHz frequency) enables robust self-engineering of geometric phase vortex masks with $m = 1$ above $U_{th} = 2.85 \text{ V}$.

As shown in Fig. 1(c), the mask is placed in the Fourier plane (P_2) of a lens (L_1 , focal length f_1) illuminated by a collimated expanded laser beam from a supercontinuum source that can be spectrally filtered on-demand using a set of bandpass interferential filters. The input pupil plane P_1 is located right before L_1 , where a metallic circular aperture with radius R_1 is placed. A second lens (L_2 , focal length f_2) placed at a distance f_2 from P_2 produces the image of the input pupil in the plane P_3 located at a distance $f_2(1 + f_2/f_1)$ from L_2 , where a metallic circular aperture with radius R_2 is placed. Ideally, full rejection of on-axis incident light is achieved when the Airy spot is centered on the vortex phase mask placed in P_2 provided that $R_2 < (f_2/f_1)R_1$ ¹² [see Fig. 1(c)]. The emulated stellar imaging is made using a third lens (L_3 , focal length f_3) by placing a camera in the observation plane P_4 located at a distance f_3 from L_3 . To date, optical vortex coronagraphy using umbilics as vortex masks have been made by adjusting the half-wave retardance criterion in the zeroth-order condition for monochromatic laser sources.^{20,21} This corresponds to birefringent phase retardation Δ set at the asymptotic value $\Delta_\infty = N\pi$, with $N = 1$, sufficiently far from the center of the umbilic defect. The axisymmetry of an umbilic with $m = 1$ imposes an optical retardance that vanishes as the distance r from the defect center tends to zero, causing the optical vortex mask to deviate from the ideal condition of uniform half-wave retardance. Its detrimental effect is managed by placing the liquid crystal mask between two crossed circular polarizers, which leads to $\sim 10^3$ peak-to-peak intensity reduction for the azimuth average coronagraphic images in P_4 as reported in Refs. 20 and 21.

Here, our sample provides similar performances for $N = 1$ (reached at $U \simeq 1.1U_{th}$) as in our previous works when polarization filtering is activated [see thin curves in Fig. 2(c)]. In other words, polarization filtering is necessary regardless of the way used (electric, photo-electric, or magnetic-electric) to create the umbilics-based mask. Once polarization filtering is removed, the coronagraphic performance drastically drops, see thick curves in Fig. 2(c). This visually can be grasped from imperfect “ring of fire” in P_3 shown in Fig. 2(b), where one can see that intensity leaks inside the re-imaged area of the input pupil plane ($r < R_1$). This is related to the fact that the size of the nonuniform central part of the liquid crystal vortex mask is not negligible compared to that of the Airy spot [see Fig. 2(a)]. Here, we show that increasing the voltage sufficiently far from U_{th} we can shrink the nonuniform central part of the mask, which makes the polarization filtering not needed. The results are shown in Figs. 2(d)–2(f) for $U \simeq 5.2U_{th}$, which corresponds to the high-order half-wave condition with $N = 11$.

The relevant quantity allowing to assess the downsizing of the nonuniform central part of the liquid crystal vortex mask is of light-matter nature. In fact, birefringent phase retardation modulation takes place along the radial coordinate in the vicinity of the center of the umbilic [see Fig. 3(a)], where the vortex mask is imaged between crossed circular polarizers as N is increased by electrical means at fixed temperature. Qualitatively, the vortex mask can be considered as being uniform at a given half-wave retardance order N at distance r larger than the radius of the last dark ring (or dark area for $N = 1$ and $N \gg 1$). Quantitatively, this is retrieved from azimuth-average radial intensity profiles by defining the radius r_1 of inhomogeneous retardance as the largest value of r satisfying $\langle I(r) \rangle_\phi = 0.95 \max_r [\langle I(r) \rangle_\phi]$. The results are shown in Fig. 3(b) at 488 and 633 nm wavelengths, see

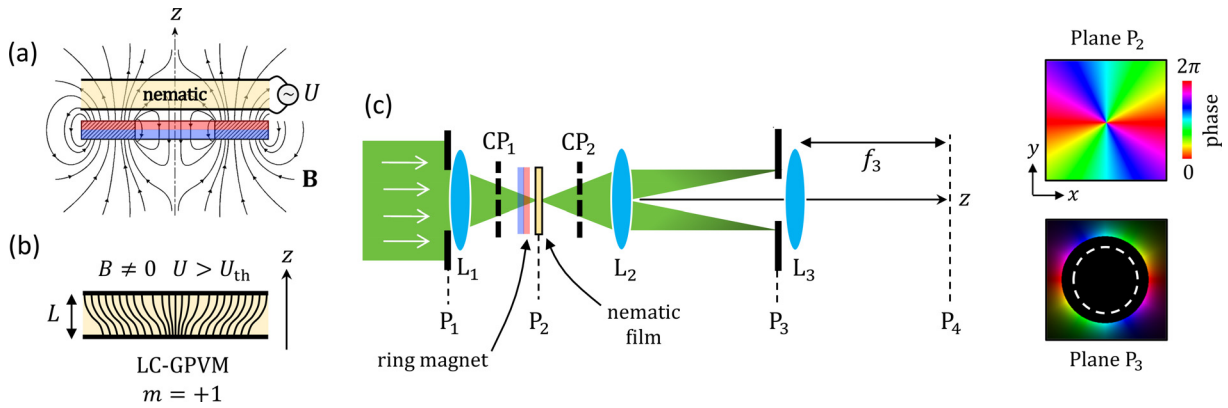


FIG. 1. (a) Illustration of the magnetic-electric configuration to generate on-demand spectrally tunable liquid crystal geometric phase vortex mask (LC-GPVM) with $m = +1$. The ring magnet (not on scale²³) is placed at a distance ~ 2 mm from the input facet of the nematic slab. (b) Side view sketch of the resulting ideally axisymmetric director field streamlines. (c) Sketch of the coronagraphic experimental setup. P_i : planes $i = (1, 2, 3, 4)$ of interest; L_i : lens $i = (1, 2, 3, 4)$ with focal length f_i ; $CP_{1,2}$: circular polarizers. Parameters: the radius of the circular aperture at P_1 is $R_1 = 1$ mm, the radius of the circular aperture at P_3 is $R_2 = 0.75R_1$, the focal lengths are $f_1 = f_2 = 200$ and $f_3 = 400$ mm. Inset at P_2 : phase map of the optical vortex mask. Inset at P_3 : calculated intensity and phase; luminance: intensity, colormap: phase. The dashed circle refers to the aperture with radius R_2 .

circle markers. The maximal odd values of N that can be reached experimentally are $N_{\max} = 19$ for $\lambda = 488$ nm and $N_{\max} = 13$ for $\lambda = 633$ nm. These values are consistent with the expected asymptotic birefringent phase retardation defined as $\Delta_\infty = 2\pi dnL/\lambda$, assuming that the director lies in the plane of the mask at all z when $\tilde{U} \gg 1$, where $\tilde{U} = U/U_{th}$. For the used liquid crystal sample, $L = 20 \mu\text{m}$ and $dn = 0.2287$ (at $\lambda = 589$ nm and $T = 20^\circ\text{C}$, manufacturer data sheet), Δ_∞ equals 18.8π at $\lambda = 488$ nm and 14.5π at $\lambda = 633$ nm. Such a trend can be grasped from Rapini’s analytical model from which the function $\Delta(r)$ can be calculated, hence $r_1 = \max_r \{ \sin^2[\Delta(r)/2] = 0.95 \}$ [see Refs. 25 and 27 for calculation details]. Analytical predictions are shown as square markers in Fig. 3(b), which offers a qualitative rather than a quantitative match with our observations. This can be

understood recalling that Rapini’s model assumes monomodal longitudinal profile for the director tilt angle θ with respect to the z axis, namely, $\theta(r, z) \propto \sin(\pi z/L)$, while experimental data support a saturation phenomenon, $\theta \rightarrow \pi/2$ everywhere, as the magnitude of the electrical torque exerted on the liquid crystal increases.

On-demand optimization ensuring high-order half-wave retardance condition and significant coronagraphic rejection without need of polarization filtering is, therefore, possible for any operating wavelength. This is illustrated in Fig. 3(c), where the applied electric field and temperature are used as tuning parameters. We reached $r_i/r_0 = (9.6 \pm 2.1) \times 10^{-2}$, where $r_0 = 0.61\lambda f_1/R_1$ is the Airy disk radius, over the wavelength range $450 \text{ nm} < \lambda < 750 \text{ nm}$ that covers almost all the visible domain.

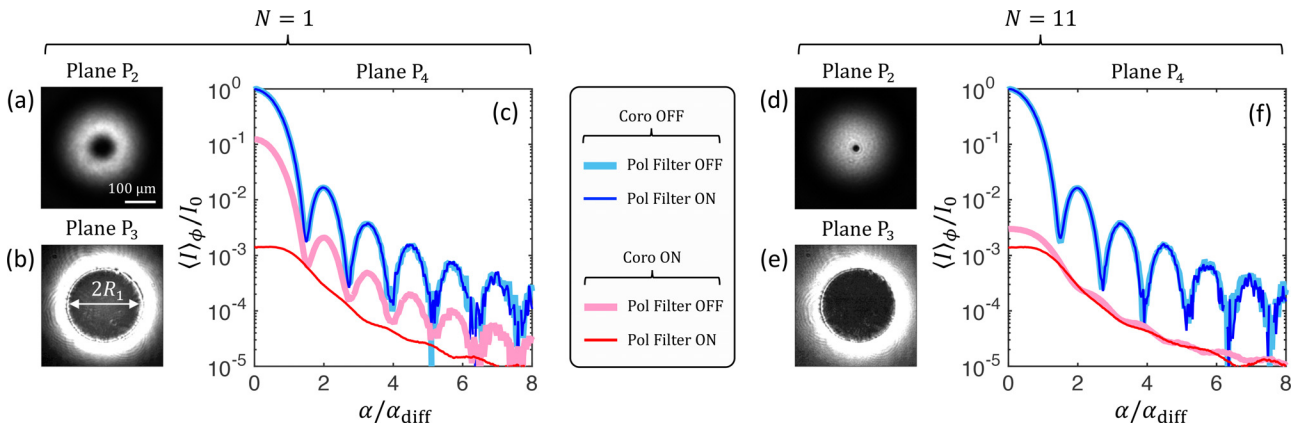


FIG. 2. Left and right parts: $\Delta_\infty = \pi (N=1)$ and $\Delta_\infty = 11\pi (N=11)$. (a) and (d) Airy spot in P_2 observed between crossed circular polarizers. (b) and (e) Ring of fire without polarization filtering in P_3 . (c) and (f) Azimuth-average angular intensity profile of the observed point-like source in P_4 with (“coro ON”) and without (“coro OFF”) activating the coronagraphic mask (i.e., by centering or laterally shifting the center of the umbilic with the Airy spot in P_2) and with (“Pol Filter ON”) and without (“Pol Filter OFF”) polarization filtering, where α is the polar angle in P_4 and $\alpha_{diff} = 0.61\lambda/R_1$ is the diffraction limit angle of the telescope. Parameters: wavelength $\lambda = 633$ nm at temperature $T = 19^\circ\text{C}$ and $U = 3.09$ V for $N = 1$ and at $T = 45^\circ\text{C}$ and $U = 14.80$ V for $N = 11$.²⁶ The corresponding pairs of images [(a) and (d) and (b) and (e)] are, respectively, recorded with equal exposure time and input light power for direct visual comparison, while (b) and (e) are overexposed to emphasize the degraded ring of fire for the lowest value of N .

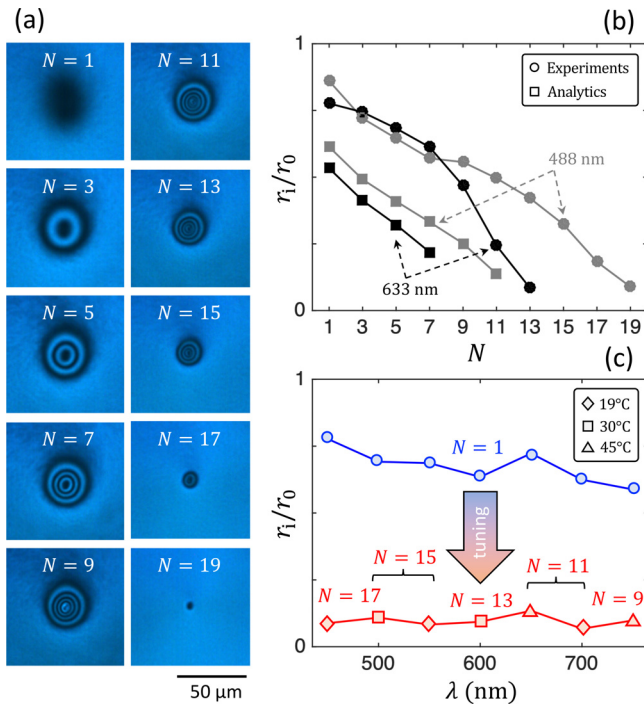


FIG. 3. (a) Images of the central part of the vortex mask observed between crossed circular polarizers using an incoherent white light source spectrally filtered at 488 nm wavelength and a 20× microscope objective with a numerical aperture NA = 0.3 at $T = 19^\circ\text{C}$. Ten orders are observed for the half-wave behavior (hence, ten odd values of N from 1 to 19) as U is increased at room temperature. (b) Measured dependence of r_i vs N at 488 and 633 nm wavelengths (circle markers) and the corresponding analytical expectations from Rapini’s model (square markers). (c) Electro-thermal tuning over the visible domain.

Noting that Rapini’s model, which is only valid for $\theta^2 \ll 1$, does not provide with a quantitative description, a more elaborated treatment is desirable. This can be achieved by relying on Landau–de Gennes free energy minimization full-numerical approach, as reviewed in Ref. 28. In contrast to Rapini’s model, a numerical approach allows to treat exactly the field-matter dielectric coupling without resorting on discarding transverse contributions to the constitutive Maxwell’s equation $\nabla \cdot \mathbf{D} = 0$. Specifically, we jointly solve the full Landau–de Gennes free energy minimization and the generalized Laplace equation $\partial_i \epsilon_{ij} \partial_j V = 0$ for the electric potential V in the liquid crystal slab associated with the boundary conditions $V(x, y, z = 0) = 0$ and $V(x, y, z = L) = U$, where ϵ_{ij} is the dielectric permittivity tensor with $i, j = (x, y, z)$ and assuming summation over double indices. Also, the numerical approach allows accounting for possible changes of nematic order in the presence of large orientational gradients and handling orientational saturation effects.²⁸

We choose a parallelepipedic simulation box with square cross section and assume fixed orientational boundary conditions at the edges of the box in all directions, where we imposed $\mathbf{n} = \mathbf{e}_z$. The free energy minimum is found by solving the Euler–Lagrange equations together with the generalized Laplace’s equation, which eventually gives the director field. A finite-difference relaxation method is used in a cylindrical domain within a computational box with the size of $750 \times 750 \times 100$ voxels, with a spatial resolution of 10 nm in all directions.

We note that computational resources prevent to address the behavior of a sample with the same dimensions as those used in the experiments. Still, it allows going beyond Rapini’s model. During the relaxation, the director field on all lattice sites is updated in each time step until the steady state is achieved, usually after a few 10^5 relaxation steps. This gives reliable results inside a cylindrical domain with radius $R = 2.5 \mu\text{m}$ for a slab of thickness $L = 0.94 \mu\text{m}$ ²⁹ [see Fig. 4(a)].

The results are shown in Fig. 4, using single elastic constant $K = 12.8 \text{ pN}$ (neglecting elastic anisotropy), $\epsilon_{\perp} = 4.33$ and $\epsilon_{\parallel} = 2.25$. In Fig. 4(b), the numerical predictions are compared to Rapini’s model (red curve) that gives $\theta_{\text{max}} = \{2(\bar{U}^2 - 1)/[1 - (\epsilon_a/\epsilon_{\parallel})\bar{U}^2]\}^{1/2}$ accounting for the single elastic constant approximation, see Eq. (13) in Ref. 25. In Fig. 4(c), the simulations clearly exhibit the appearance of high-order odd Fourier components for the longitudinal profile of the director as \bar{U} increases, namely, $\theta(r, z) \propto \sum_{n \text{ odd}} \theta_n \sin(n\pi z/L)$ with $n > 1$. Eventually, Fig. 4(d) displays the radial profile of the director reorientation in the mid-plane of the liquid crystal slab, which we found to moderately depart from the universal profile provided by Rapini’s model as \bar{U} increases.

In summary, active enhancement of the intrinsic coronagraphic rejection of spectrally tunable liquid crystal geometric phase vortex masks has been demonstrated, although the spectral bandwidth of the tunable operating wavelength is so far limited to $\sim 1\%$. The approach relies on electrically induced reduction the size of the non-ideal central region of the vortex mask and is equally applicable to all wavelengths.

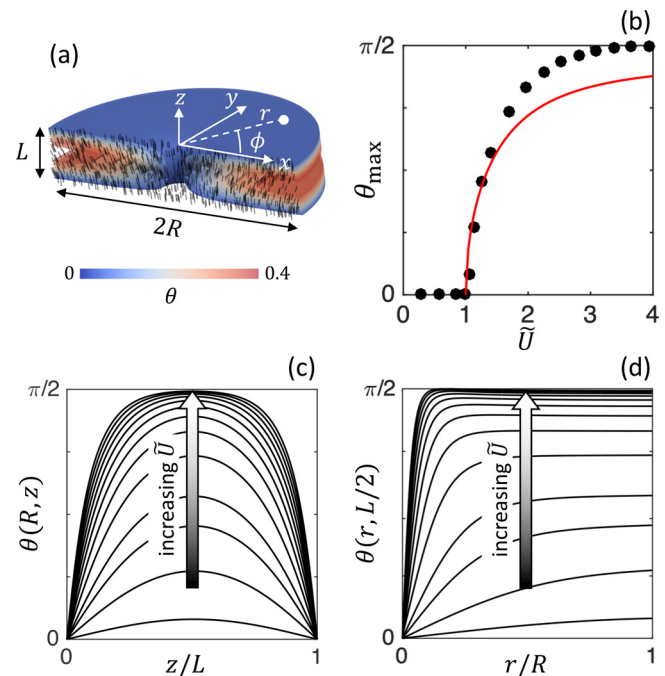


FIG. 4. (a) Simulated 3D director field profile of an umbilic defect at $\bar{U} = 1.12$. The black segments refer to the director orientation and color levels refer to the value of the director tilt angle θ . (b) Maximal director reorientation angle vs the reduced applied voltage. Black markers: simulations. Red curve: Rapini’s model. (c) and (d) Saturation of the longitudinal and transverse reorientation profiles according to the 13 values above threshold reported in panel (a): $\bar{U} = 1.05, 1.12, 1.26, 1.40, 1.68, 1.96, 2.24, 2.52, 2.81, 3.09, 3.37, 3.65, \text{ and } 3.93$.

Of course, obtained raw contrast $\sim 10^{-3}$ remains modest compared to very recent record values $\sim 10^{-9}$ using high-tech solid-state polymer liquid crystal geometric phase mask from BEAM Engineering manufacturer at the High Contrast Imaging Testbed NASA's facility.¹⁷ However, we stress that our nature-assisted liquid-state approach comes with a low level of constraints making it suitable for a wide use by the amateur astronomy community.

N.K. and E.B. thank the support from the Conseil Régional de Nouvelle Aquitaine (Project HELIXOPTICS). U.M, M.R., and S.Ž acknowledge the funding from Slovenian research agency ARRS, Grant Nos. P1-0099, N1-0195, and J1-2462, and from EU ERC AdG LOGOS.

AUTHOR DECLARATIONS

Conflict of Interest

The authors have no conflicts to disclose.

Author Contributions

Nina Kravets: Formal analysis (lead); Investigation (lead); Methodology (equal); Writing – review & editing (equal). **Urban Mur:** Formal analysis (equal); Investigation (equal); Writing – review & editing (equal). **Miha Ravnik:** Supervision (supporting); Writing – review & editing (equal). **Slobodan Žumer:** Supervision (supporting); Writing – review & editing (equal). **Etienne Brasselet:** Conceptualization (lead); Formal analysis (equal); Methodology (equal); Supervision (lead); Writing – original draft (lead); Writing – review & editing (equal).

DATA AVAILABILITY

The data related to the reported findings are available from the corresponding author upon reasonable request.

REFERENCES

- R. Bhandari, "Polarization of light and topological phases," *Phys. Rep.* **281**, 1–64 (1997).
- Z. Bomzon, G. Biener, V. Kleiner, and E. Hasman, "Space-variant Pancharatnam–Berry phase optical elements with computer-generated subwavelength gratings," *Opt. Lett.* **27**, 1141 (2002).
- G. Biener, A. Niv, V. Kleiner, and E. Hasman, "Formation of helical beams by use of Pancharatnam–Berry phase optical elements," *Opt. Lett.* **27**, 1875 (2002).
- M. Honma and T. Nose, "Liquid-crystal Fresnel zone plate fabricated by microrubbing," *Jpn. J. Appl. Phys.* **44**, 287 (2005).
- L. Marrucci, C. Manzo, and D. Paparo, "Optical spin-to-orbital angular momentum conversion in inhomogeneous anisotropic media," *Phys. Rev. Lett.* **96**, 163905 (2006).
- E. Karimi, B. Piccirillo, E. Nagali, L. Marrucci, and E. Santamato, "Efficient generation and sorting of orbital angular momentum eigenmodes of light by thermally tuned q-plates," *Appl. Phys. Lett.* **94**, 231124 (2009).
- B. Piccirillo, V. D'Ambrosio, S. Slussarenko, L. Marrucci, and E. Santamato, "Photon spin-to-orbital angular momentum conversion via an electrically tunable q-plate," *Appl. Phys. Lett.* **97**, 241104 (2010).
- N. Tabirian, H. Xianyu, and E. Serabyn, "Liquid crystal polymer vector vortex waveplates with sub-micrometer singularity," in *Proceedings of IEEE Aerospace Conference* (IEEE, 2015), pp. 1–10.
- B. Lyot, "A study of the solar corona and prominences without eclipses," *Mon. Not. R. Astron. Soc.* **99**, 580–594 (1939); available at <https://adsabs.harvard.edu/pdf/1939MNRAS...99..580L>
- F. Roddier and C. Roddier, "Stellar coronagraph with phase mask," *Publ. Astron. Soc. Pac.* **109**, 815 (1997).
- G. Foo, D. M. Palacios, and G. A. Swartzlander, "Optical vortex coronagraph," *Opt. Lett.* **30**, 3308–3310 (2005).
- D. Mawet, P. Riaud, O. Absil, and J. Surdej, "Annular groove phase mask coronagraph," *Astrophys. J.* **633**, 1191–1200 (2005).
- D. Mawet, E. Serabyn, K. Liewer, C. Hanot, S. McEldowney, D. Shemo, and N. E. O'Brien, "Optical vectorial vortex coronagraphs using liquid crystal polymers: Theory, manufacturing and laboratory demonstration," *Opt. Express* **17**, 1902–1918 (2009).
- D. Mawet, E. Serabyn, K. Liewer, K. Burruss, J. Hickey, and D. Shemo, "The vector vortex coronagraph: Laboratory results and first light at palomar observatory," *Astrophys. J.* **709**, 53–57 (2010).
- E. Serabyn, D. Mawet, and R. Burruss, "An image of an exoplanet separated by two diffraction beamwidths from a star," *Nature* **464**, 1018–1020 (2010).
- O. Absil, D. Mawet, M. Karlsson, B. Carlomagno, V. Christiaens, D. Defrère, C. Delacroix, B. Femenía Castellá, P. Forsberg, J. Girard, C. A. Gómez González, S. Habraken, P. M. Hinz, E. Huby, A. Jolivet, K. Matthews, J. Milli, G. Orban de Xivry, E. Pantin, P. Piron, M. Reggiani, G. J. Ruane, G. Serabyn, J. Surdej, K. R. W. Tristram, E. Vargas Catalán, O. Wertz, and P. Wizinowich, "Three years of harvest with the vector vortex coronagraph in the thermal infrared," *Proc. SPIE* **9908**, 99080Q (2016).
- G. Ruane, A. Riggs, E. Serabyn, W. Baxter, C. M. Prada, D. Mawet, M. Noyes, P. Poon, and N. Tabirian, "Broadband vector vortex coronagraph testing at NASA's high contrast imaging testbed facility," *Proc. SPIE* **12180**, 1218024 (2022).
- E. Serabyn, C. M. Prada, P. Chen, and D. Mawet, "Vector vortex coronagraphy for exoplanet detection with spatially variant diffractive waveplates," *J. Opt. Soc. Am. B* **36**, D13–D19 (2019).
- D. S. Doelman, E. H. Por, G. Ruane, M. J. Escuti, and F. Snik, "Minimizing the polarization leakage of geometric-phase coronagraphs with multiple grating pattern combinations," *Publ. Astron. Soc. Pac.* **132**, 045002 (2020).
- A. Aleksanyan and E. Brasselet, "Vortex coronagraphy from self-engineered liquid crystal spin-orbit masks," *Opt. Lett.* **41**, 5234–5237 (2016).
- A. Aleksanyan, N. Kravets, and E. Brasselet, "Multiple-star system adaptive vortex coronagraphy using a liquid crystal light valve," *Phys. Rev. Lett.* **118**, 203902 (2017).
- B. Piccirillo, E. Piedipalumbo, L. Marrucci, and E. Santamato, "Electrically tunable vector vortex coronagraphs based on liquid-crystal geometric phase waveplates," *Mol. Cryst. Liq. Cryst.* **684**, 15–23 (2019).
- The Nickel-plated Neodymium (grade N50) ring magnet has internal and external radii $R_{\text{int}} = 2$ and $R_{\text{ext}} = 6$ mm, respectively, and height $H = 6$ mm. Its magnetization is directed along the z axis and is associated with a pull force of ~ 32 N (manufacturer datasheet).
- E. Brasselet, "Tunable high-resolution macroscopic self-engineered geometric phase optical elements," *Phys. Rev. Lett.* **121**, 033901 (2018).
- A. Rapini, "Umbilics: Static properties and shear-induced displacements," *J. Phys.* **34**, 629–633 (1973).
- Importantly, we keep $U < 18$ V in order to prevent from electrical destabilization related to the imperfections of the liquid crystal sample, while the temperature is adapted to preserve the half-wave retardance condition $\Delta_{\infty} = N\pi$ with N odd integer.
- E. Brasselet, "Tunable optical vortex arrays from a single nematic topological defect," *Phys. Rev. Lett.* **108**, 087801 (2012).
- M. Ravnik and S. Žumer, "Landau–de Gennes modelling of nematic liquid crystal colloids," *Liq. Cryst.* **36**, 1201–1214 (2009).
- Technically, three layers of voxels are used on the top and bottom parts of the computational box in order to ensure in the numerical formulation the strong boundary conditions, while 125 voxels in the radial direction are found necessary to screen the effects of finite extension of the nematic slab in the (x, y) plane.